Shockwave generation by a semiconductor bridge operation in water

E. Zvulun, G. Toker, V. Tz. Gurovich, and Ya. E. Krasik
Physics Department, Technion, Haifa 32000, Israel

(Received 25 March 2014; accepted 9 May 2014; published online 23 May 2014)

A semiconductor bridge (SCB) is a silicon device, used in explosive systems as the electrical initiator element. In recent years, SCB plasma has been extensively studied, both electrically and using fast photography and spectroscopic imaging. However, the value of the pressure buildup at the bridge remains unknown. In this study, we operated SCB devices in water and, using shadow imaging and reference beam interferometry, obtained the velocity of the shock wave propagation and distribution of the density of water. These results, together with a self-similar hydrodynamic model, were used to calculate the pressure generated by the exploding SCB. In addition, the results obtained showed that the energy of the water flow exceeds significantly the energy deposited into the exploded SCB. The latter can be explained by the combustion of the aluminum and silicon atoms released in water, which acts as an oxidizing medium. © *2014 AIP Publishing LLC*. [http://dx.doi.org/10.1063/1.4878958]

I. INTRODUCTION

Many applications, such as the ignition of different types of fuel and pyrotechnic and explosive materials, require reliable igniters. Among the different types of igniter, the semiconductor bridge (SCB) can be considered the best candidate for such types of application. SCB, envisioned and patented by Hollander, Jr,[1] is a silicon device, fabricated using microelectronic surface micromachining methods. The device is built onto a silicon wafer and comprises a polycrystalline, highly doped, silicon bridge. The bridge is connected via gold wires, ultrasonically bonded to two metallic lands. This device enables one to avoid the disadvantages of the exploding wire and hot-wire igniters. Namely, it was found that, using a doped semiconductor resistor, one can achieve reproducible and reliable ignition of different explosives without using primary explosives and boosters.[2] Although the patent publication suggests that SCB operation is based on the controllable resistance of the device versus the temperature as the source mechanism of ignition, in later publications[3,4] a plasma-explosion mechanism was reported. The first stage of the SCB explosion is characterized by fast heating of the bridge from room temperature to the melting point by the discharge current.[3,5] During this stage, the SCB undergoes a transition from a predominant extrinsic semiconductor resistivity behavior to an intrinsic one in the high temperature range, just below the melting temperature. Namely, an initial increase in the temperature of the SCB leads to almost complete ionization of the doping atoms, which supply charge carriers to the conduction band. Thus, during this stage of the discharge, the charge carrier density changes drastically with temperature, allowing a rise in the conductivity and resulting in a conductor in which the temperature coefficient of resistivity is negative. Simultaneously with the process of the increase in these charge carriers in the conduction band, an increase in the vibration of the lattice also occurs. The latter leads to a decrease in the mobility of the charged carriers, and moreover, this vibration (and, respectively, scattering of carriers on this vibration) becomes the dominant process that causes the increase in the SCB resistance versus the temperature. An additional increase in the temperature of the SCB up to the melting point leads to a fast decrease in the resistance due to the liberation of all four valence electrons of silicon to the conduction band. Further, continuing energy deposition causes a fast increase in the resistance versus temperature, as in common conductors. The last stage of the SCB operation is characterized by the evaporation of the liquid silicon with doped material and the formation of a low-ionized plasma with a rather low temperature in the range of 2000 K–7000 K.[6–9]

Two models were suggested to explain the ignition of energetic materials using SCB. Both models consider the plasma that is formed as a result of SCB explosion as a main source of energy that is transferred to the energetic material. However, while the first model considers a heat transfer to the explosive from the plasma,[3,13] the second model[10] is based on the generation of high pressure by expanding plasma. The parameters of the plasma (density, temperature, and expansion velocity) were investigated using different electrical, optical, and spectroscopic methods.[6–9] The majority of the experiments with SCB electrical explosion were performed either in air at atmospheric pressure or in a sealed bridge with explosive material pressed onto it. It is understood that, because of the high level of the electromagnetic noise, the parameters of the plasma, and in particular the pressure evolution, cannot be measured in the vicinity of the exploded SCB. In addition, the analysis of the spectroscopic data obtained in collision, non-uniform in space, and transient plasma could contain some uncertainties.

Murphy *et al.*[10] measured the pressure of an SCB explosion in air, using a shadow imaging technique via a Schlieren optical scheme. Using a similar technique, in the present experiments we studied the operation of an SCB immersed in water. Namely, the expansion of the exploded bridge and generated shockwave (SW) were measured for different amplitudes of the discharge current and different geometries of the SCB. The measured velocities of the SCB expansion of the SCB and SW propagation were used for

calculating the pressure at the bridge using hydrodynamic modeling. This method of measurement of the pressure is a non-disturbing method and requires only time- and space-resolved optical diagnostics and hydro-dynamic simulations coupled with the equation of state (EOS) of water. Interferometry experiments confirmed the results of the time-of-flight shadow imaging.

II. EXPERIMENTAL SETUP AND DIAGNOSTICS

The tested SCB devices were fabricated at Rafael–Advanced Defense Systems Ltd, Microsystems Department Fab. The process of fabrication was performed using a standard 4″ silicon wafer having a 2 μm thermal oxide layer (see Fig. 1). CVD silicon was deposited on the thermal oxide layer, resulting in a 2 μm polycrystalline silicon layer (i.e., polysilicon). A phosphorus diffusion doping process was performed in order to bring the layer to the highly doped state. The polysilicon was patterned and dry-etched using fluorine-based reactive plasma (RIE process). In the next step of the fabrication process, a 2 μm layer of aluminum was deposited on the surface of the wafer via vacuum evaporation and patterned using chlorine-based reactive plasma etching. The wafer was then rinsed, protected with a protective tape, and diced into individual devices.

Three types of SCB device differing in width and length were used in this study with lateral dimensions 71 μm × 200 μm, 106 μm × 300 μm, and 142 μm × 400 μm. The electrical resistance of the SCB samples was kept at a constant 1.1 ± 0.1Ω, by keeping the ratio between the length and width constant. The SCB devices were wired onto a header, which has two pins with glass-to-metal insulation. The header is attached to a connector placed at the bottom of the deionized water-filled stainless steel chamber. The chamber has four azimuthally symmetrical side sapphire windows for optical observations and a top PMMA window. The SCB was placed at the axis of the chamber and optical windows.

The pulsed power source that supplies the discharge current to the exploding SCB consists of a high-voltage capacitor connected to the SCB via a fast IGBT switch (Behlke HTS31-320). The latter is protected from overloads by a high-voltage fast diode assembly. The application of this switch allows one to control the duration and synchronization of the discharge current using a control 5 V square voltage pulse with adjustable width (≥100 ns). This circuit allows one to operate the device with currents of up to 3.2 kA without applying current-limiting resistors. The discharge current I was measured using an Ion-Physics calibrated current transformer. Two Tektronix high-impedance probes were used to measure the voltage V across the SCB by subtracting the voltage measured at the input and the output of the SCB lands. The inductance L of the circuit was determined in a short-circuit shot and this value was used to calculate the resistive voltage across the SCB, $V_r = V - L(dI/dt)$ and, respectively, the dynamic resistance of the SCB, $R(t) = V_r(t)/I(t)$, the deposited power, $P = I(t) \cdot V_r(t)$, and energy, $W = \int_0^\tau I(t)V_r(t)dt$. The parameters of the discharge electrical circuit were calibrated using a low-inductance 3 Ω carbon resistor placed instead of the SCB, where the measured current waveform was fitted as $I(t) = I_0(1 - e^{-tR/L})e^{-t/RC}$. Using this fitting procedure, the parameters of the circuit were found: inductance $L = 1.09$ μH and total circuit capacitance $C = 12.1$ μF.

Shadow imaging[11] was used for recording the instantaneous position of the front of the underwater SW, generated by the SCB explosion. A Diode pumped solid state (DPSS) laser diode ($\lambda = 532$ nm) was used for illuminating the SW with following focusing of the laser beam on the entrance window of a fast framing 4QuikE intensified camera. The camera operated in a sequence of three frames with a time delay between frames of 300 ns and frame duration of 5 ns (see Fig. 2). The spatial resolution of the optical setup was determined using a calibration ruler resulting in a resolution of 10 μm/pixel. The obtained data were used for calculating the time-of-flight of the SW generated by the SCB explosion. The shadow imaging of the exploding SCB and generated SW was done from the side and front views. In the case of the front view, a beam splitting cube was used to pass the light from the laser onto the SCB device.

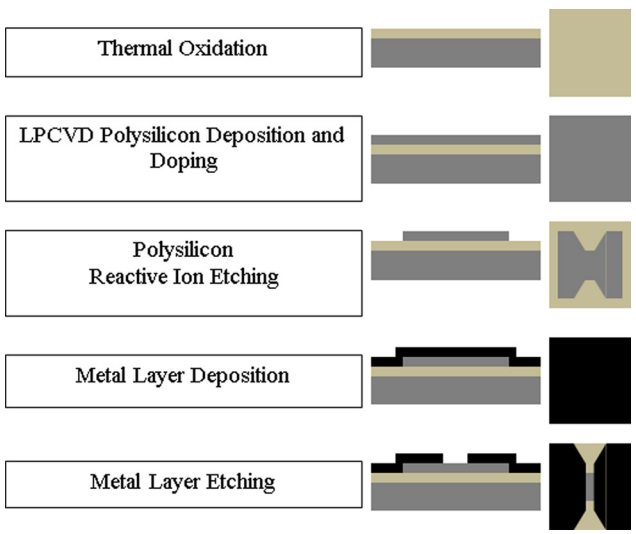

FIG. 1. Fabrication process flow of the SCB.

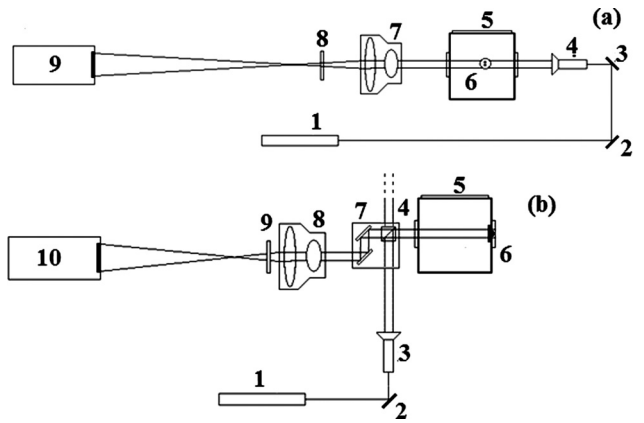

FIG. 2. Shadow imaging scheme. (a) Side-view: (1) DPSS green laser; (2) and (3) 1″ aluminized mirrors; (4) beam expander; (5) water-filled chamber; (6) wire-bonded SCB; (7) objective lens; (8) interference filter for $\lambda = 532 \pm 3$ nm; (9) 4QuikE camera. (b) Top-view: (1) DPSS CW laser; (2) 1″ aluminized mirrors; (3) collimator; (4) beam splitter; (5) water chamber; (6) SCB; (7) mirror array; (8) objective lens; (9) interference filter; (10) 4QuikE camera.

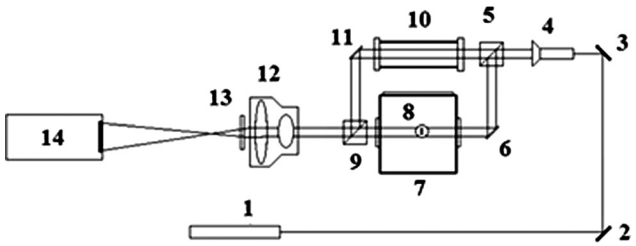

FIG. 3. Reference beam interferometry: (1) DPSS CW laser; (2), (3), and (6) 11. 1″ aluminized mirrors; (4) collimator; (5) and (9) beam-splitting cubes; (7) water-filled chamber; (8) SCB; (10) compensating cell; (12) objective lens, (13) interference filter; (14) 4QuikE camera.

In a few experiments, in order to correlate electrical measurements with the plasma ignition, fast photography images of the light emission from the plasma formed during SCB explosion in air were taken. In these experiments, a Specialized 8 single shot SIMX camera (Specialized-Imaging company) with Questar 1QM objective lens was used. In this setup, an SCB was placed on a plastic holder and a copper strip was pressed on the aluminum pads to form the electrical contact.

A more quantitative technique in the field of visualization and measurement of phase objects is reference beam interferometry.[11,12] In the present research, the Mach-Zehnder scheme was applied (see Fig. 3). Namely, using a beam splitter, a laser beam ($\lambda = 532\,\text{nm}$) was divided into two beams, which pass through two different cells. The first cell is the experimental chamber with the exploding SCB and the second cell is the reference cell containing water and being of the same length as the first cell. The difference in optical paths results in an interference image, which can be described as[11] $f(x,y) = E_0^2\{1 + \cos[\Delta\phi(x,y) + (2\pi/d)x]\}$. Here, $\Delta\phi = (2\pi/\lambda)\int_\Gamma n d\ell$ is the phase difference over the length of the ray's path, where n is the spatially dependent refractive index. In the calculation of the optical path (see Fig. 4) using a basic ray tracing Matlab code, the Eikonal equation[17,21]

$$\frac{d}{ds}\left[n(r)\frac{d\mathbf{x}}{ds}\right] = \nabla n \tag{1}$$

was applied. Here, $ds = c_0 dt$ is the unit path and c_0 is the sound velocity in water at normal conditions; the refractive index $n(r)$ was considered as a linear function of the radius, $n(r) = n_1 - n_2(r/R)$, where R is the radius of the SW sphere, and n_1 and n_2 are the constant and slope parameters of the refraction index, respectively. The equations in spherical

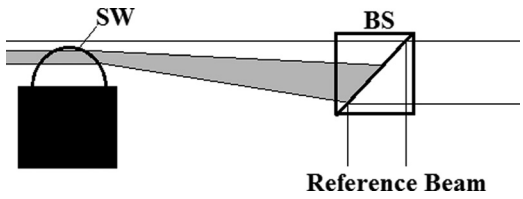

FIG. 4. Laser ray passing through the spherical object and refracting into the beam splitter. BS is the beam splitter.

coordinates were solved numerically. Initial conditions were taken at the location where the ray path enters the SW. The initial propagation angle of each ray was taken with respect to the ray refraction at the SW front. Further, the ray's path behind the SW sphere was considered in order to estimate which part of the sphere image would interfere with the reference beam (see Fig. 4).

For a low compression of water, when the dimensionless density $\delta = \rho/\rho_0 \approx 1$, where ρ and ρ_0 are the density of water behind the SW front and in non-disturbed water, respectively, one can find $\delta(r)$ using the approximate relation between the change in the refractive index and density:[14] $\Delta n(r) = 0.3255[\delta(r) - 1]$. Further, the pressure was calculated using the EOS for water $p(r) = A[\delta^n - 1]$, where $A = 3 \times 10^8\,\text{Pa}$ is the constant and $n = 7.15$ is the isentropic index for water. Finally, the Mach number of the SW propagation can be calculated by taking the value of the $\delta(r)$ behind the SW front as $M = \left[\delta(\delta^n - 1)/n(\delta - 1)\right]$.

In addition, this optical scheme allows one to measure the velocity D of the SW front by measuring the angle μ of the Mach cone in the wake of the advancing semi-spherical front of the SW generated by the SCB explosion as $D = c_0 \sin^{-1}\mu$.

III. EXPERIMENTAL RESULTS

A. Electrical measurements

SCB explosions were performed with a discharge current amplitude varied in the range of 70–300 A and pulse duration in the range of 1 μs–10 μs. The typical waveforms of the discharge current and voltage and the calculated dissipated power, energy, and SCB's resistance shown in Fig. 5 are similar to those obtained in earlier experiments with analogous SCB explosions in air.[13] The two peaks in the voltage waveforms are related to the increase in the SCB resistance when the mobility of the electrons from the doping atoms decreases because of the increased thermal lattice vibration (first voltage peak) and the vaporization of the

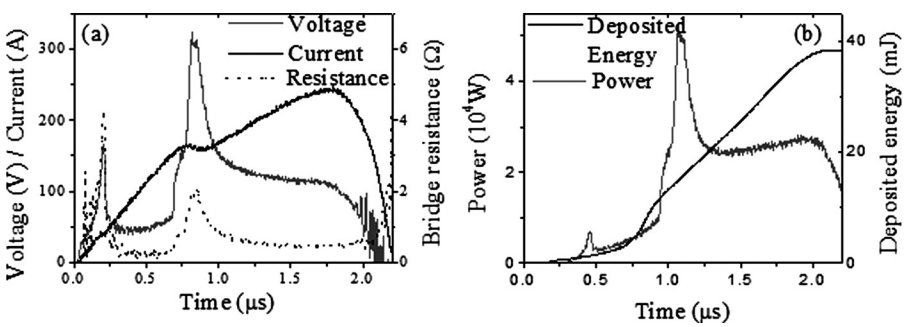

FIG. 5. (a) Typical waveforms of the discharge current, voltage, and resistance of the SCB; (b) temporal evolution of the deposited power and energy. Charging voltage of the capacitor was 300 V, current pulse duration of 2 μs. SCB: width of 300 μm and length of 106 μm.

bridge (second voltage peak). An almost constant voltage with increasing discharge current between these two peaks corresponds to the time interval when the bridge experiences solid state–liquid phase transitions with temperature increasing above melting point, and when four valence electrons become free and participate in the current conductivity.

At the time of the second voltage peak, one obtains a decrease in the discharge current. At that time, the energy density deposited into the bridge reaches $\omega_\nu = (4.2 \pm 0.1) \cdot 10^4\,\mathrm{J/cm^3}$, which is sufficient to evaporate the doped layer (a rough estimate showed that one requires $\omega_\nu = 2.2 \cdot 10^4\,\mathrm{J/cm^3}$). This time delay τ_d in the appearance of the second peak in the discharge voltage with respect to the start of the current is related to the maximum resistivity of the exploding SCB. The decrease in the second peak voltage is caused by ionization of the evaporated layer and formation of rather resistive plasma that continues to conduct current with increasing amplitude at almost constant discharge voltage. The latter is related to the decrease in the plasma resistivity due to the increase in the plasma temperature by Joule heating of the plasma by the discharge current. Qualitatively similar waveforms of the discharge current and voltage were obtained for other geometries of the SCB tested. It was found that the value of τ_d decreases with the increase in the amplitude of the discharge voltage (current) for each SCB tested (see Fig. 6). In addition, for the constant discharge voltage, the value of τ_d increases with increasing bridge volume. Qualitatively, the latter results are predictable. However, as one can see in Fig. 6, a ~4 times increase in the discharge current (for the same SCB) or 2 times decrease in the bridge's cross-section areas leads to only a ~2 times decrease in the value of τ_d (see Fig. 6). In addition, it was found that the energy density $\omega_v \approx 4.2 \cdot 10^4\,\mathrm{J/cm^3}$ deposited into a specific SCB at τ_d was almost constant for different charging voltages and, respectively, different amplitudes of the discharge current. These quantitative results contradict well-accepted conditions for conductor explosion, which begins when $\tau_{\exp} \propto g_0 S^2 I^{-2}$ is satisfied, where S is the cross-section area of the bridge and g_0 is the specific action, which is defined experimentally for each material.[16] Thus, one can suppose that additional processes, for instance, heat transfer to the Si material and water and vaporization of the Si and Al lands, could play a significant role in SCB explosion at that time scale. Finally, after the second peak in the voltage, the deposition energy rate was constant for charging voltages $\leq$200 V, and thus, the deposited energy versus time was $\propto t$, which is consistent with the results presented in Refs. 5 and 13. However, it was found that at larger discharge currents ($I > 250$ A for 142 μm × 400 μm SCB, and $I > 150$ A for 106 μm × 300 μm and 71 μm × 200 μm SCB) this dependency varied with both the energy and volume of the SCB to be $\propto t^\alpha$, where $1 < \alpha < 2$. For instance, the energy deposition was found to be $\propto t^2$ for a discharge voltage of 400 V ($I \approx 350$ A) and with SCB sizes of 71 μm × 200 μm and 106 μm × 300 μm. These data also indicate that the vaporization processes of the Si or Al lands could be involved in SCB explosion.

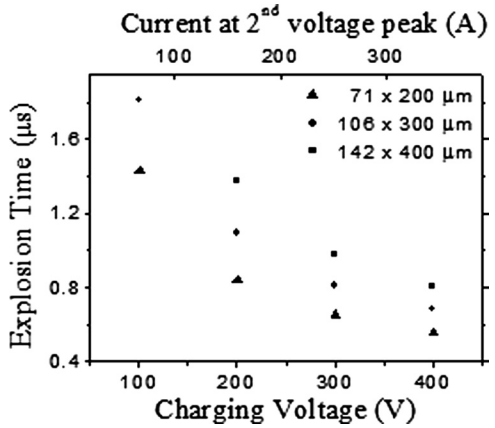

FIG. 6. The time of the appearance of the 2nd peak in the discharge voltage versus the capacitor charging voltage for different cross-section areas of the SCB.

B. Shock wave shadow-imaging

The first shadow images were obtained as single exposure frames, at different values of τ_d in order to determine the beginning of the SCB explosion. Electrical measurements show that the second voltage peak already occurs after the explosion of the SCB explosion (see Fig. 5). Thus, these images were taken around this time τ_d in order to test this assumption. The images showed that indeed the visible SW front in the vicinity ($\leq 20\,\mu$m) of the SCB becomes resolvable at $\tau_{\exp} \approx \tau_d - 100$ ns, i.e., prior to the time of the second voltage peak. Thus, this time $\tau_{\exp}$ is henceforth referred to as the explosion of the SCB and the SW formation point. At that time, the bridge undergoes its phase transformation leading to the formation of low-ionized plasma,[5,13] the fast expansion of which leads to the formation of SW in water.[18–20]

Next, multi-frame shadow images (three images each of 5 ns duration of a single frame and with a 300 ns time delay between frames) were obtained to calculate the velocity of the SW propagation in water (see Fig. 7). The velocity was measured for three types of SCB sample, each with three different charging voltages of the primary stored capacitor. One can see that each single image of SW consists of three well-distinguished waves. The generation of these waves can be related to the sequence of phase transitions experienced by exploding SCB, namely, solid-liquid-gaseous-plasma phases, which occur with some time delay between each other. The

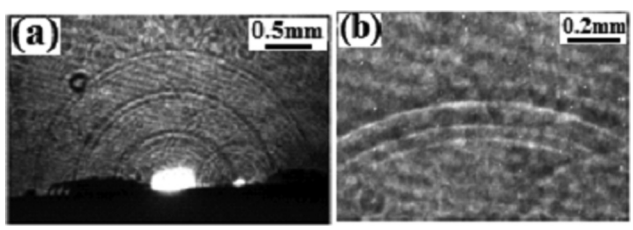

FIG. 7. (a) Typical shadow image of exploding 106 μm × 300 μm SCB and generated SW. The current amplitude is 150 A at the time of the second peak in the discharge voltage. Frame duration is 5 ns and time delay between frames is 300 ns. (b) Zoom of the SW front. Frame duration is 10 ns and the image was obtained at the time of 250 ns with respect to the second peak on the discharge voltage.

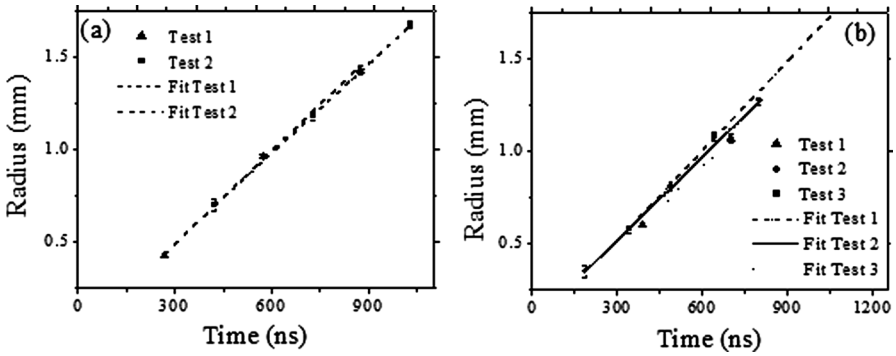

FIG. 8. Radius of the SW versus time for the case of (a) $106\,\mu m \times 300\,\mu m$ SCB and (b) $71\,\mu m \times 200\,\mu m$ SCB explosions at a charging voltage of 300 V.

estimation of the exact time when the SCB generates the SW could contain a rather large time error. Therefore, the velocity of the SW propagation was measured using a differential method, namely, $V_{sw} = \Delta r/\Delta t$, where Δr and Δt are the distance between the SW front and time interval between the frames, respectively. The error for the Δr measurement was estimated as ± 2 pixels, and the Δt error was estimated as the exposure time of the camera. This analysis indeed showed that the values of the velocities of these three waves differ from each other. For instance, in the case of the $106\,\mu m \times 300\,\mu m$ SCB and charging voltage of 300 V, the first, outer wave is characterized by constant velocity $V_1 = (1.5 \pm 0.05)\cdot 10^5$ cm/s, which is almost equal to sound velocity in non-disturbed water, $C_0 = 1.47\cdot 10^5$ cm/s, while the second wave has a slightly larger velocity $V_2 = (1.52 \pm 0.02)\cdot 10^5$ cm/s, and the third wave can be characterized by expansion velocity $V_3 = (1.60 \pm 0.05)\cdot 10^5$ cm/s. Similar results were obtained for explosions of other types of SCB samples and for other charging voltages. These estimates are in agreement with the suggestion that these waves are generated at different times corresponding to the phase transitions of the bridge during the SCB explosion. Nevertheless, even the fastest third wave has Mach number $M \approx 1.1$ and it can be considered a weak SW. The unexpected result was that the velocity of this weak SW was found to be constant versus the radial distance. In Fig. 8, examples of the dependences of the radial position of the front of the SW versus the time are shown for the case of the $71\,\mu m \times 200\,\mu m$ SCB and $106\,\mu m \times 300\,\mu m$ SCB explosions at a charging voltage of 300 V. The error seen in Fig. 8 is the result of the linear fitting calculated error in addition to the radius measurement and time error.

Another, also unexpected result was that the change in the charging voltage in the range of 100 V–400 V resulting in the change in the discharge current (70–350) A, at the time of the second peak in the voltage does not noticeably effect the average value of the SW velocity. Namely, the SW velocity remains constant within the range of error bars (see Fig. 9). Let us note that, in spite of the relatively large error bars, the sound velocity in non-disturbed water, also shown in Fig. 9, always remains smaller that the SW velocity. Here, the error in the velocity of the SW propagation consists of two factors. The first factor is related to the accuracy of the measurements and does not exceed $\pm 4\%$, remaining at a constant value for all measurements. The second factor is related to the non-reproducibility of the measured velocity of the SW obtained in different explosions of SCBs having the same dimensions. Here, the increase in the charging voltage and, respectively, in the discharge current, leads to some decrease in the "scattering" of the velocities measured for different explosions. One can see that, for instance, in the case of a charging voltage of 300 V, for the same $300\,\mu m \times 106\,\mu m$ SCB, the velocity of the SW measured at different shots was varied in the range $(1.59–1.68)\cdot 10^5$ cm/s, which corresponds to the water compression $\delta = \rho/\rho_0 = (1.028–1.033)$ and pressure $(6.55–7.84)\cdot 10^7$ Pa behind the front of the SW, respectively. Taking into account that water prevents surface breakdown (one requires ~300 kV/cm to obtain breakdown in water), other factors not related to the explosion of the SCB and parasitic breakdowns should be considered to explain such non-reproducibility in the velocity of the generated SW. Let us note that, for each specific SCB explosion, the time-of-flight data showed that the velocity of the SW remains constant. Moreover, images obtained after the current termination have shown a similar behavior of SW propagation. Namely, the SW propagation velocity remained the same up to 600 ns with respect to the current cut-off, i.e., to the termination of the electrical energy deposition.

The experiments in which we attempted to take multiple exposure front view shadow images were not successful, i.e., we failed to obtain images of the SW of sufficiently good quality (see Fig. 10). This occurs because most of the area of the SW is darkened by the metallic lands made of

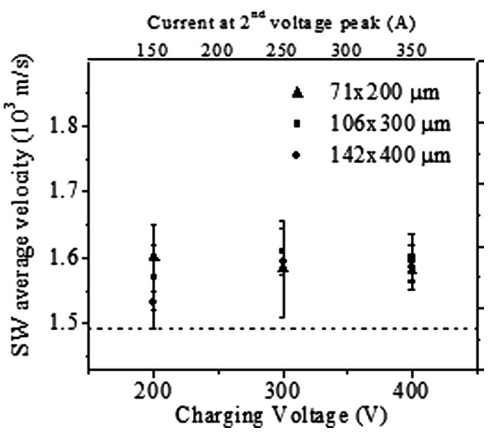

FIG. 9. Summary of the SW velocity measured in the cases of the explosion of three different SCBs and for three values of charging voltages using three exposures of the camera with a single frame duration of 5 ns and time delay between frames of 300 ns. Each dot represents an average of three identical SCB explosions.

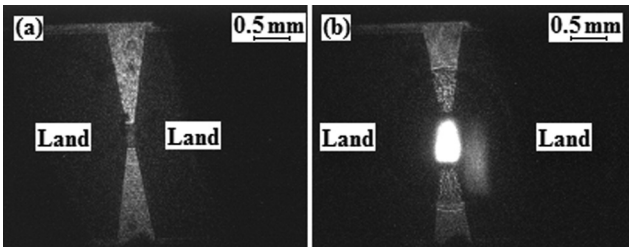

FIG. 10. Front view shadow images of a 300 μm × 106 μm SCB. Frame duration of 5 ns. (a) Before the SCB operation. (b) Time delay of 0.5 μs with respect to the beginning of the discharge current explosion. Charging voltage is 300 V. The amplitude of the discharge current is 180 A at the time of the second peak in the discharge voltage.

vacuum-deposited aluminum that has a high level of roughness, and thus, cannot serve as a mirror. The area that is most visible is the bare silicon surface above and below the bridge. Nevertheless, one can see that the form of the SW front is not a perfect sphere. These front and side images allow one to estimate the dimensions of the bright emission spot ~0.4 mm in length, ~0.25 mm in width, and ~0.25 mm in height. This spot represents the expanding plasma that generates SW. One can estimate roughly the radial and longitudinal velocities of the plasma spot expansion as $V_{rad} \sim 2.5 \cdot 10^4$ cm/s and $V_{lon} \sim 4 \cdot 10^4$ cm/s. The difference in the values of these velocities can be related, for instance, to the evaporation and ionization of the lands or to the magnetic pressure of the discharge current, which prevents radial expansion of the Plasma Cavity (PC).

Additional information concerning the time and space evolution of the SCB explosion was obtained with the SIMX camera setup. In these experiments, explosions of SCB were performed in air at normal pressure. The front-view images, seen in Fig. 11, show a non-uniform bridge explosion. Namely, early in the explosion, the brighter light emission is obtained from the location of the edges of the Al lands, and later from the side edges of the bridge. The side-view images, seen in Fig. 12, show the bridge explosion, starting with two hot spots at the edges of the bridge. The brighter plasma light emission at the locations of the contact Al land–doped Si can be explained qualitatively by the contact potential differences due to the different resistivity of the Al lands and doped Si. In addition, brighter plasma emission at the edges of the bridge can be explained by the higher current density at that location due to the edge effect, i.e., the stronger electric field. Another interesting observation is that the side-view images show the expansion of the plasma plume upwards with a velocity of ~2 × 10^5 cm/s and that the

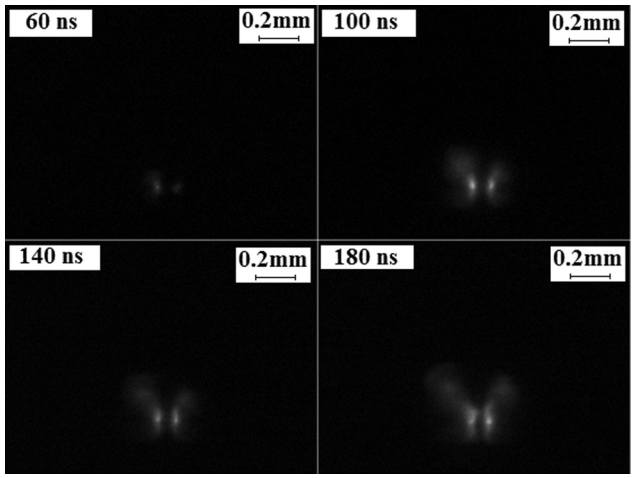

FIG. 12. Side-view snapshots taken with time delay between frames (frame duration of 5 ns) of 40 ns from the 89 μm × 250 μm SCB explosion in air. Discharge current of 60 A.

expansion of the plasma is not isotropic: two upward plumes of the plasma that diverged from each other were obtained. The latter can be explained by the fact that a part of the discharge current is carried out by these plumes, leading to magnetic repulsion between these plumes.

C. Reference beam interferometry

The reference beam interferometry of the exploding SCB in water was performed with a charging voltage of $\varphi_{ch} = 200$ V (maximal current amplitude at the time of second peak in the discharge voltage of 150 A). At larger charging voltages, the interference images obtained were too difficult to interpret. A typical reference beam interferometry image, obtained in the case of the explosion of a 71 μm × 200 μm SCB ($\varphi_{ch} = 200$ V), is shown in Fig. 13. The image was produced from the side-view using a single exposure of 5 ns duration at 700 ns after the time of explosion. The SW front is visible when this method is used, as the fringes bend greatly in the front of the shock. At the side of the expanding wave, a line disturbance corresponding to a Mach-cone with an angle of 72.65° can be seen. The latter allows one to estimate the SW front velocity to be $V_{SW} = (1.046 \pm 0.02) \cdot c_0$, which coincides well with the time-of-flight measurement data. Thus, in simulations of an interferometric image (see Sec. II), the value $M = 1.026$, which gives a pressure behind the SW front of $2.5 \cdot 10^7$ Pa, was considered as the boundary condition; this value of M results in the best fit of the simulated and experimentally obtained fringes. Carried out simulations (see

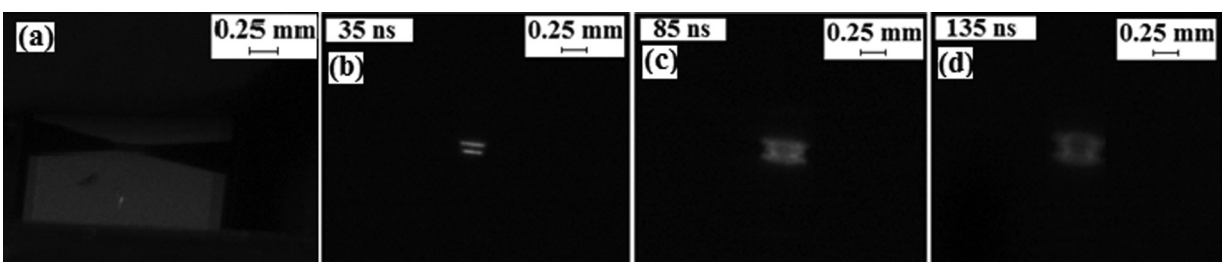

FIG. 11. (a) SCB: 89 μm × 250 μm. (b)–(d) Snapshots, taken with time delay of 50 ns between frames. Discharge current amplitude is of 60 A.

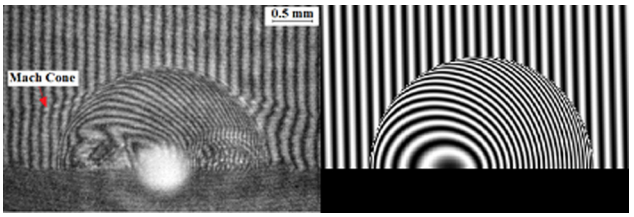

FIG. 13. Left image: experimentally obtained interferometry image with a Mach cone expanding from a propagating semi-spherical shock-front, imaged using reference beam interferometry method. Discharge voltage of 200 V. Time delay is 2 μs. Frame duration is 5 ns. Right image: calculated interferometry image.

Sec. II) showed that, because light rays bend as they pass the compressed water, only a small part ($\sim$9% of the semi-sphere radius) of the light rays overlap the reference beam (see Fig. 4). Thus, only these rays were considered in the simulated interference image. The results of these simulations showed that the value of the pressure of $4 \cdot 10^7$ Pa is already reached at a distance of only 9% of the sphere radius. Here, let us note that, assuming the same linear dependence of the refractive index $\Delta n(r) = 0.3255[\delta(r) - 1]$, the simulated pressure in the vicinity of the exploding SCB should be as large as $(1.1 \pm 0) \cdot 10^8$ Pa. Thus, the results of interferometry agree rather well with the results of time-of-flight measurements and Mach cone measurements.

IV. DISCUSSION

The main purpose of the present research is the determination of the pressure generated by an exploding SCB. The analysis of time-of-flight measurements, Mach cone, and interferometry images showed that, in the case of a charging voltage of 200 V, the SCB explosion results in a value of the SW Mach number of $M_f = 1.046$, which gives the pressure behind the SW front of $\sim 2.5 \times 10^7$ Pa. In addition, it was found that the velocity V_{SW} of this SW is almost constant versus the radial distance studied and the energy input to the SCBs of different geometries (see Fig. 8). The latter results were rather unexpected. In order to explain them, let us consider a model of self-similar SW propagation. Laser shadow imaging and interferometry have shown an approximately semi-spherically expanding front of the SW having its origin on the bridge surface with a rather small expansion velocity, allowing one to use the EOS of water,

$$p(\delta) = P_0 + A[\delta^n - 1], \tag{2}$$

where P_f and P_0 are the pressure behind the SW front and in non-disturbed water, respectively. Using time normalized to the speed of sound velocity $\tau = c_0 t$ and assuming that all the parameters of the water flow depend on a self-similar variable $\xi = r/\tau$, a self-similar SW propagation can be described as[15]

$$(M - \xi)\frac{dM}{d\xi} = -\delta^{n-1}\frac{d\ln\delta}{d\xi}; (M - \xi)\frac{d\ln\delta}{d\xi} = -\frac{dM}{d\xi} - \frac{2M}{\xi}. \tag{3}$$

The boundary conditions for M and δ are determined at the SW front, which is characterized by the self-similar variable $\xi_f = V_{SW}/c_0 = M_f$, where V_{SW} is the velocity of the SW in the laboratory coordinate system. The experimental results showed that this velocity V_{SW} remains almost constant during the time interval of the energy deposition, which can be related to the expansion of the exploded SCB. The values of M_f and δ_f at the SW front are not independent values and depend on each other. Indeed, using mass and momentum conservation laws, the velocity V_{SW} of the SW and velocity of the water flow U behind the SW are[15]

$$V_{SW} = \frac{1}{\rho_0}\sqrt{\frac{P_f - P_0}{(1/\rho_0 - 1/\rho_f)}};$$
$$U = \sqrt{(P_f - P_0)(1/\rho_0 - 1/\rho_f)}. \tag{4}$$

Using the EOS of water (see Eq. (2)), one can determine the density δ_f, pressure P_f, and U behind the SW front for known values of V_{SW}. Knowing these values at the radial position of the SW front, one knows also the value of $\xi_f = V_{SW}/c_0 = M_f$. Thus, using these boundary conditions one can solve self-consistently the system of Eq. (3) and, respectively, determine the density, velocity, and pressure distributions of water flow versus the radius.

It is convenient to present Eq. (4) using sound velocity $Z(\delta) = \delta^{(n-1)/2}$ in the compressed water behind the SW front as

$$M_f = \sqrt{\frac{({\delta_f}^n - 1)\delta_f}{n(\delta_f - 1)}}; \quad M = \sqrt{({\delta_f}^n - 1)(\delta_f - 1)/n\delta_f}, \tag{5}$$

where $M = U/C_0$ and $\delta_f = \rho_f/\rho_0$. Now, using $\delta = Z^{2/n-1}$ one can re-write the system of Eqs. (3) as

$$\left[\frac{(M - \xi)^2}{Z^2} - 1\right]\frac{dM}{d\xi} = \frac{2M}{\xi};$$
$$\left[\frac{(M - \xi)^2}{Z^2} - 1\right]\frac{dZ}{d\xi} = -\frac{M(\gamma - 1)(M - \xi)}{\xi}. \tag{6}$$

Now, for known values of P_f, V_{SW}, and ρ_f behind the SW front, one can solve the system of Eq. (6), thus determining distributions of water flow parameters behind the SW front. This model considers the self-similar flow of water generated by an expanding semi-spherical cavity whose velocity corresponds to the self-similar argument ξ_p. It is understood that the boundary of the expanding cavity should have a velocity equal to the velocity of the water in the vicinity of this boundary. This means that $M(\xi_p) = \xi_p$ and that the pressure in the water should have maximum value at the boundary of the cavity. Thus, the self-similar flow of the water in the semi-sphere determines the expansion of the cavity and pressure at its boundary if one knows parameters of the SW.

The numerical solution of the system of Eq. (6) determines the parameters of the cavity for an experimentally measured value of M_f. For instance, in the case of the exploding 300 μm $\times$ 106 μm SCB (charging voltage of 300 V and maximal discharge current $I \approx 250$ A), the average value of the SW front Mach number was $M_f \approx 1.074$, remaining constant during time $\Delta t \approx 1.2\,\mu$s. Behind the front of the

SW, the pressure and density reach $P_f \approx 8 \times 10^7$ Pa and $\delta_f \approx 1.035$, respectively. The propagation of the SW is sustained by the expanding semi-spherical cavity consisting of ionized material, which is formed by the electrical explosion of the SCB, and the cavity boundary r_p is assumed to be at the location where the maximum pressure is achieved. The results of the simulations give the dimensionless velocity of the piston expansion $\xi_p \approx 0.477$. The radial distribution of the pressure between the SW front and the cavity and water flow velocity for different values of V_{SW} obtained in experiments are shown in Fig. 14. One can see that the pressure and velocity of the water flow behind the front of the SW increases as one moves from the front of the SW, characterized by self-similar argument $\xi_f = M_f$, toward the boundary of the expanding cavity, characterized by self-similar argument ξ_P, where one determines the velocity M_P of the cavity expansion. Let us note that the ratio between V_{SW} and the velocity of the cavity V_p is $V_{SW}/V_p = \xi_f/\xi_p = r_f/r_p \approx 2.3$. In the experiment, the ratio between the SW and cavity radii was also $\sim$2.3 for $V_{SW} = 1.56 \times 10^5$ cm/s. The latter showed that our suggestion that the piston boundary should be defined at the location of the maximum pressure is correct. Thus, one obtains that the pressure at the piston boundary reaches $P(\xi_p) \approx 4.9 \times 10^8$ Pa, which is $\sim$6.5 times larger than the pressure behind the SW front.

Now, let us calculate the energy of a semi-spherical water layer between the SW front, determined by ξ_f, and the boundary of the cavity, determined by ξ_p:

$$E(t) = 2\pi(c_0 t)^3 \int_{\xi_p}^{\xi_f} \xi^2[\varepsilon_k(\xi) + \varepsilon_i(\xi)]d\xi. \tag{7}$$

Here, the kinetic and potential energy density of the unit of the volume of water $\varepsilon_k = \rho(r,t)U^2(r,t)/2$ and $\varepsilon_i = A\{(n-1)^{-1}[(\delta)^{n-1} - 1] + [\delta - 1]\}$ (Ref. 15) using solutions of Eq. (7) are written in the form

$$\varepsilon_k(\xi) = \rho_0 c_0^2 \delta(\xi) M^2(\xi)/2;$$
$$\varepsilon_i(\xi) = \left[\frac{c_0^2 \rho_0 \delta}{n}\right]\left\{\frac{1}{(n-1)}\left[\delta(\xi)^{n-1} - 1) - (1 - 1/\delta(\xi)\right]\right\}. \tag{8}$$

Results of these simulations showed that for the time $t \approx 800$ ns, one obtains $E \approx 30$ mJ. On the other hand, at that time the total energy delivered to the exploded SCB is $E \sim 20$ mJ. Experiments with exploding wires[16] showed that $\sim$20%, i.e., $\sim$4 mJ, of the total energy delivered to the wire can be transferred to the generated water flow. The latter is $\sim$7.5 times smaller than the calculated energy of the water flow. The apparent contradiction can be explained if one can consider that this additional energy is deposited because of the partial combustion of Al electrodes and Si. Indeed, combustion of 1 g of either Al or Si results in an energy of 3 kJ/g and 15 kJ/g, respectively, being realized. Thus, one requires only a few μg of Al and Si to be combusted to obtain this additional energy of the piston, which provides the obtained velocity of the SW propagation.

In addition, the results of the simulations showed that the power delivered to the water flow, which enters the SW at $r \approx 1.36 \times 10^{-1}$ cm and propagates with $M_f \approx 1.09$, is $w \approx 8 \times 10^4$ W. However, this value of the power is almost two times larger than the maximum power of the electrical discharge, which is 4.4×10^4 W. This result also indicates that the process of the generation of the SW and water flow behind it requires an additional source of energy and not only expansion of the exploding SCB.

Finally, one can see from Eq. (7) that the energy of the water layer increases $\sim t^3$. Following the same proportionality increases the work produced by the expanding cavity. Indeed, the force and work produced by the cavity is $F(t) = 2\pi r_p^2(t) P_p$ and $dA = F(t)dr_P(t)$, respectively. Taking into account that $r_P(t) = V_P t$, one obtains $A(t) = 2\pi P_P V_P^3 t^3/3$. However, the Volt-Ampere characteristic of the discharge showed only a linear dependence of the deposited energy into the exploding SCB at charging voltages $\leq$300 V ($I \leq 250$ A). This dependence $A(t) \propto t^3$ requires additional discussion. The experiments showed that the SCB electrical explosion is accompanied by the formation of a plasma layer with a time-dependent surface area. Let us assume that the rate of the plasma particles generation is $dN/dt \propto S(t)$, where $S(t)$ is the area of the plasma layer in the vicinity of the base. In this case, one can assume that its area $S(t) \propto t^2$ for the constant velocity of this layer's expansion along the base. The latter results in proportionality of the ablation of the surface material to the area covered by this plasma layer. Thus, one obtains that the total number of the plasma particles inside the expanding cavity will be $N(t) \propto t^3$. This description assumes that the main part of the energy deposited into the discharge is going to the ablation and ionization of the base atoms and molecules, as well as to water molecule ionization. The following collision process leads to thermalization between plasma particles. In this case, the

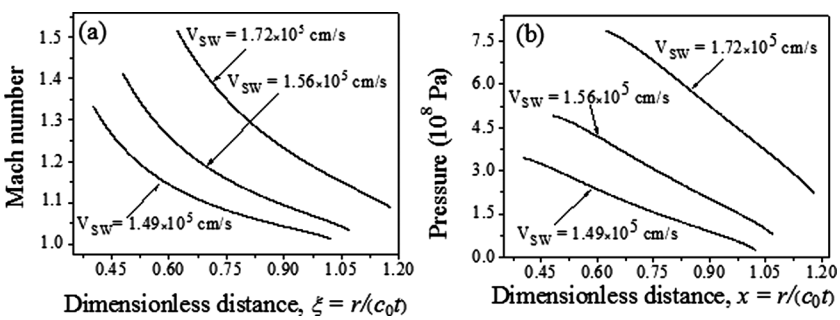

FIG. 14. (a) Simulated distributions of the flow velocity in Mach numbers (a) and pressure (b) behind the SW front for different velocities of the SW front propagation. The location of the SW front is at r = 1.5 mm. For this specific location of the SW, the location of the "piston" is 0.79 mm for $V_{SW} = 1.72 \times 10^5$ cm/s, 0.67 mm for $V_{SW} = 1.56 \times 10^5$ cm/s, and 0.58 mm for $V_{SW} = 1.49 \times 10^5$ cm/s.

pressure inside the cavity, whose volume increases as $Q \propto t^3$, will be $P \approx kTN(t)/Q(t) = const$, which corresponds to our self-similar solution.

The results of the self-similar model predict that the pressure at the cavity boundary will be significantly larger (for instance ~6.5 times larger for $V_{SW} = 1.56 \cdot 10^5$ cm/s) than the pressure behind the SW front. The model assumes constant velocities of the SW propagation and expansion of the cavity formed by the exploded SCB. This assumption is based on experimental data showing constant velocity of the SW propagation within an experimental error bar of ~4%. Thus, it is useful to estimate the change in the velocity of the SW during its propagation using a model of a weak SW[22] when water compression $\delta \approx 1 + \varepsilon$, where $\varepsilon \ll 1$ The increase in the pressure versus the decrease in radius can be expressed as $P \approx P_f(r_f/r)$. In experiments, the radius of the expanding cavity was $r_P \approx r_f/3$, which predicts a pressure at the cavity boundary ~3 times larger than the pressure behind the SW front. In addition, using this model one obtains that the velocity of the SW and the pressure behind the SW front are $M_f = V_{SW}/c_0 \approx 1 + \varepsilon_f/2$ and $P_f \approx \rho_0 c_0^2 \varepsilon_f$, respectively. In this case, the compression of water versus the radius is $\varepsilon \approx \varepsilon_f(r_f/r)$. The latter results in the dependence of the water flow Mach number on the radius of the SW propagation,

$$M_f(r) \approx 1 + \varepsilon_f r_f/2r, \tag{9}$$

and the time-dependent radius of the SW,

$$r(t) = c_0 t + (\varepsilon_f r_f/2)\ln(t/t_0).$$

Here, t_0 is the time of the beginning of the SCB explosion, when the radius of the SW is $r_f = c_0 t_0$. For the three values of V_{SW}, $(1.49 \pm 0.059) \times 10^3$ m/s, $(1.56 \pm 0.062) \times 10^3$ m/s, and $(1.72 \pm 0.069) \times 10^3$ m/s at $r_f \approx 1.5 \times 10^{-3}$ m, considered in the self-similar model, the model of a weak SW gives values of $\varepsilon_f = \delta_f - 1$ as 0.011, 0.032, and 0.081 respectively. The change in the Mach values of the water flow between $r_p \approx 0.5$ mm and $r_f \approx 1.5$ mm can be estimated as $\Delta M_f \approx \varepsilon_f$ which gives the change in the SW front velocity ΔV_f: 22 m/s, 66 m/s, and 172 m/s, respectively. One can see that, in fact, only for $V_{SW} = (1.72 \pm 0.069) \times 10^3$ m/s does the change in the velocity of the SW exceed the error bar of experimental measurements significantly, thus justifying the application of the self-similar model in this case.

Now, let us estimate the energy of water flow using the model of a weak SW. The internal energy density can be expressed as $E_i \approx c_0^2 \varepsilon/2$, where the radial distribution of the water compression is $\varepsilon \approx \varepsilon_f(r_f/r)$. Thus, the total internal energy in the water flow between the SW and expanding cavity is

$$W_i = 2\pi \int_{r_p}^{r_f} E_i(r) r^2 dr \approx 2\pi \rho_0 c_0^2 \varepsilon_f^2 r_f^2 (r_f - r_p). \tag{10}$$

For the considered values of ε_f, 0.011, 0.032, and 0.081, one obtains $W_i \approx 0.008$ J, 0.062 J, and 0.386 J, respectively. Here, we accounted for the fact that the kinetic energy of the water flow is roughly equal to its potential energy. In addition, using experimental data that the $V_{SW} \propto Const$ within the time interval $\Delta t \approx 1$ μs and is close to c_0, one obtains that the radius of the cavity changes as $r_p \approx V_p t$, where $V_p \approx c_0/3$. In this case, the increase in the energy in the spherical water layer between $r_f(t)$ and $r_p(t)$ at $t \le T = 1$ μs can be written as

$$W(t) = \frac{2}{3}\pi \rho_0 c_0^3 \varepsilon_f^2(T) r_f^2(T) t. \tag{11}$$

Here, $\varepsilon_f(T)$ and $r_f(T) \approx 1.5 \times 10^{-3}$ m are the values of the internal energy density and SW radius at $t = T$, respectively. Let us note that in this model of a weak SW, which is valid in the range $r_f \ge r \ge r_p$, the energy of the water flow increases $\propto t$, similar to the increase in electrical energy delivered to the discharge, which is equal to ~0.02 J (power $\omega \approx 2 \times 10^4$ W). Thus, one can see that, in this particular case, the efficiency of the electrical energy transfer to the energy of the water flow is $k \approx 0.2$.

During the earlier stages of the SCB explosion, when the radius of the cavity is comparable to the size of the SCB, the pressure behind the SW is rather large and the model of the weak SW cannot be applicable. Nevertheless, in order to estimate the pressure at the boundary of the cavity, we will suppose that the efficiency of the transfer of the energy delivered to the SCB to the work $A(t)$ of the water flow generation does not exceed $k \approx 0.2$:

$$A(t) = \frac{2\pi}{3}\int_0^R P(r) r^2 dr = kwt. \tag{12}$$

In this case, the radial dependence of the pressure will be

$$P(r) = \frac{3kw}{2\pi r^2(t)(dr/dt)}. \tag{13}$$

Taking into account that the velocity of the cavity expansion remains constant $dr/dt \approx c_0/3$, one obtains a pressure at the boundary cavity–water $P(R) = 9kw/2\pi r^2 c_0$, which results in a pressure of $\sim 4 \cdot 10^8$ Pa at radius $r \approx 10^{-4}$ m, comparable with the typical size of the SCB. The latter agrees satisfactorily with the result of the self-similar model.

V. SUMMARY

We fabricated SCB devices and operated the devices under high charging voltage conditions. The electrical measurements of the operating SCBs were compared to previous results obtained by other groups, and it was shown that the SCBs parameters were, in fact, similar to those obtained in previous works.

Using shadow imaging and reference beam interferometry, the velocity of the SW propagation and distribution of the density of water between the SW and expanding boundary of the exploded SCB were obtained. These experimental results, together with a self-similar water flow model, were used to calculate the pressure that is generated by the exploding SCB.

The experimental and simulation results showed that the energy of the water flow exceeds significantly the energy

deposited into the exploded SCB. It is supposed that the source of the additional energy could be combustion of aluminum and silicon atoms released in gas-form during their oxidation in contact with the water, which acts as an oxidizing media.

ACKNOWLEDGMENTS

We wish to thank Rafael—Advanced Defense Systems for the collaboration, and the Microsystems department for the SCB device fabrication and further experimental assistance. We also thank Mr. G. Goldstein for the experimental assistance, and S. Gleizer and A. Levin for technical assistance. This research was supported in part by the Center for Absorption in Science, Ministry of Immigrant Absorption, State of Israel.

[1]L. E. Hollander, Jr., U.S. patent 3366055 (30 Jan 1968).
[2]R. Bickes, M. Grubelich, S. Harris, J. Merson, and J. Weinlein, in Proceedings of 31st AIAA Joint Propulsion Conference (San Diego, CA, USA, 1995), AIAA 95-2549.
[3]D. A. Benson, M. E. Larsen, A. M. Renlund, W. M. Trott, and R. W. Bicks, J. Appl. Phys. **62**, 1622 (1987).
[4]R. W. Bicks, Jr. and A. C. Schwarz, U.S. patent 4708060 (24 Nov 1978).
[5]M. Liu and X. Zhang, IEEE Trans. Plasma Sci. **38**, 2812 (2010).
[6]Z. Lin, H. Yan, F. Hongyan, and Z. Shunguan, in *Proceedings of International Seminar Propellants, Explosives and Pyrotechnics* (Kunming, China, 2009), p. 652.
[7]K. N. Lee, M. I. Park, S. H. Choi, C. O. Park, and H. S. Uhm, Sens. Actuators, A **96**, 252 (2002).
[8]H. Feng, L. Zhang, S. Zhu, R. Wu, Y. Li, and R. Shen, IEEE Trans. Plasma Sci. **37**, 1830 (2009).
[9]J. Kim, E. Schamiloglu, B. Martinez-Tovar, and K. C. Jungling, IEEE Trans. Instrum. Meas. **44**, 843 (1995).
[10]M. J. Murphy, S. A. Clarke, A. C. Munger, and K. A. Thomas, in *Proceedings of 36th International Pyrotechnics Seminar*, Rotterdam, the Netherlands, 2009. Retrieved from http://www.osti.gov/scitech/servlets/purl/990790.
[11]H. W. Liepmann and A. Roshko, *Elements of Gasdynamics* (John Wiley & Sons, 1957), p. 153.
[12]G. Pretzler, H. Jager, and T. Neger, Meas. Sci. Technol. **4**, 649 (1993).
[13]K. D. Marx, R. W. Bickes, Jr., and D. E. Wackerbarth, Characterization and Electrical Modeling of Semiconductor Bridges, SAND97-8246 UC-706 (1997).
[14]P. Schiebener, J. Straub, J. M. H. Levelt-Sengers, and J. S. Gallagher, J. Phys. Chem. Ref. Data **19**, 677 (1990).
[15]Y. B. Zel'dovich and Yu. P. Raizer, *Physics of Shock Waves and High-Temperature Hydrodynamic Phenomena* (Academic Press, New York, 1967), p. 785.
[16]V. Ts. Gurovich, A. Grinenko, Ya. E. Krasik, and J. Felsteiner, Phys. Rev. E **69**, 036402 (2004).
[17]T. C. Poon and T. Kim, *Engineering Optics with Matlab* (World Scientific Publishing Co., Singapore, 2006), p. 7.
[18]A. Grinenko, A. Sayapin, V. Tz. Gurovich, S. Efimov, J. Felsteiner, and Ya. E. Krasik, J. Appl. Phys. **97**, 023303 (2005).
[19]A. Grinenko, V. Tz. Gurovich, A. Saypin, S. Efimov, V. I. Oreshkin, and Ya. E. Krasik, Phys. Rev. E **72**, 066401 (2005).
[20]D. Veksler, A. Sayapin, S. Efimov, and Ya. E. Krasik, IEEE Trans. Plasma Sci. **37**, 88 (2009).
[21]M. Born and E. W. Wolf, *Principles of Optics* (Pergamon, New York, 1980), p. 121.
[22]L. D. Landau and E. M. Lifshitz, *Fluid Mechanics* (Pergamon, New York, 1987), p. 327.